

Renal-Clearable Porphyrinic Metal–Organic Framework Nanodots for Enhanced Photodynamic Therapy

Huan Wang,^{†,‡,§} Dongqin Yu,^{†,‡,§} Jiao Fang,[§] Changcui Cao,[§] Zhen Liu,^{*,†,‡} Jinsong Ren,^{*,†,‡} and Xiaogang Qu^{*,†,‡}

[†]State Key Laboratory of Rare Earth Resources Utilization and Laboratory of Chemical Biology, Changchun Institute of Applied Chemistry, Chinese Academy of Sciences, Changchun, Jilin 130022, People's Republic of China

[‡]University of Science and Technology of China, Hefei, Anhui 230029, People's Republic of China

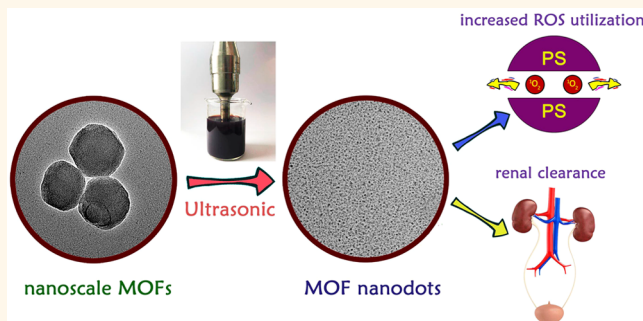
[§]Beijing Advanced Innovation Center for Soft Matter Science and Engineering, Beijing University of Chemical Technology, Beijing 100029, People's Republic of China

^{*}School of Stomatology, Jilin University, Changchun, Jilin 130021, People's Republic of China

Supporting Information

ABSTRACT: Nanoscale porphyrinic metal–organic frameworks (NMOFs) have emerged as promising therapeutic platforms for the photodynamic therapy (PDT) of cancer in recent years. However, the relatively large sizes of current NMOFs ranging from tens to hundreds of nanometers usually lead to inefficient body clearance and unsatisfactory PDT effect, thus amplifying their long-term toxicity and restricting their further usage. To overcome these shortcomings, herein, ultrasmall porphyrinic metal–organic framework nanodots (MOF QDs) prepared from NMOFs are rationally synthesized *via* a facile method and used as renal-clearable nanoagents for the enhanced PDT of cancer. Compared with the precursor NMOFs, our well-prepared MOF QDs can generate 2-fold effective toxic reactive oxygen species (ROS) upon the same light irradiation and greatly decrease the inefficacy of PDT caused by the inefficient use of ROS generated from the interior of NMOFs. Meanwhile, the IC₅₀ value of ultrasmall MOF QDs is nearly one-third that of NMOFs, and *in vivo* results demonstrate that our MOF QDs exhibit better PDT efficacy than NMOFs under the same treatment owing to their overcoming the limited ROS diffusion distance. Significantly, these ultrasmall MOF QDs show efficient tumor accumulation and rapid renal clearance *in vivo*, indicating their potential in biomedical utility. Last but not least, comprehensive investigations of long-term toxicity of these MOF QDs well demonstrate their overall safety. Therefore, this study will offer valuable insight into the development of safe and high-performance PDT nanoplatfroms for further clinical translation.

KEYWORDS: metal–organic framework, nanodots, enhanced photodynamic therapy, renal clearance; long-term toxicity



Metal–organic frameworks (MOFs) have attracted increasing interest in the fields of gas storage/separation, catalysis, and nonlinear optics due to their distinctive properties including large surface areas, tunable pore sizes, and versatile architectures.^{1–6} Recently, tremendous effort has been devoted to the development of nanoscale MOFs for biomedical usages.^{7–11} In particular, by integrating photosensitizers (PSs) in the periodic arrays, nanoscale porphyrinic MOFs (NMOFs) have been well designed and used as promising therapeutic nanoagents for the photodynamic therapy (PDT) of cancer.^{12–19} These NMOFs can directly incorporate PSs as efficient building units, providing a high loading capacity of PSs to generate

highly cytotoxic reactive oxygen species (ROS), especially singlet oxygen (${}^1\text{O}_2$), under light irradiation.^{12,13} By taking advantages of the relatively isolated PSs in the well-defined structure of NMOFs, the aggregation-induced self-quenching effect of PSs can be well avoided.^{12,13,20} Moreover, the porous nature of porphyrinic NMOFs also facilitates the free diffusion of dioxygen and ${}^1\text{O}_2$ in and out of the frameworks through the channels, therefore increasing the availability of the PSs.²¹

Received: May 7, 2019

Accepted: August 13, 2019

Published: August 13, 2019

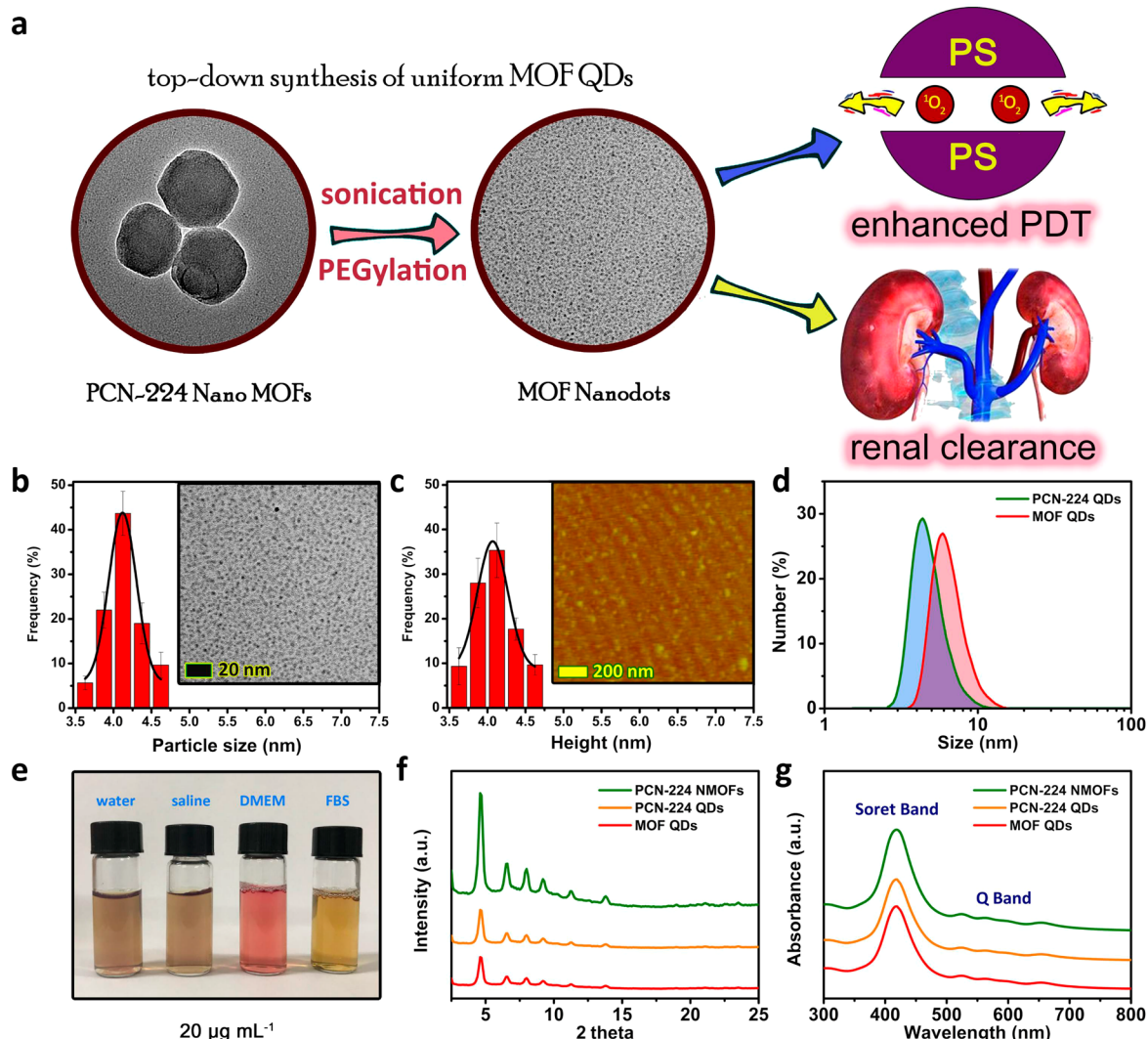


Figure 1. Schematic illustration of the rational design of MOF QDs and their usage as renal-clearable nanoagents for the enhanced PDT of cancer (a). TEM image (b) and AFM image (c) of MOF QDs. Hydrodynamic diameters of PCN-224 QDs and MOF QDs (d). Photograph of MOF QDs dissolved in different solutions (e). XRD patterns (f) and UV-vis spectra (g) of PCN-224 NMOFs, PCN-224 QDs, and MOF QDs.

Although promising, several drawbacks of current NMOF-based PDT systems still remain and thus restrict their medical usage and further clinical translation. First, NMOFs with a diameter range from tens to hundreds of nanometers can be highly taken up by the reticuloendothelial system (RES) after systemic administration, leading to a post long-term retention in the body and potential amplification of toxicity.²² Second, $\cdot\text{O}_2$ generated from the interior of NMOFs with a diameter over 20 nm cannot totally diffuse out of the frameworks effectively to process the anticancer function since the $\cdot\text{O}_2$ will be quenched within 10 nm of diffusion distance.^{23–28} Third, the sustained release of unwanted metal ions and toxic organic ligands from those NMOFs with insufficient stability after systemic administration usually induces threatened toxicity *in vivo*.^{15,29–31} Against the above battles, it is essential to develop more effective MOF-based platforms with efficient renal clearance, high ROS utilization efficacy, and high stability for the PDT of cancer.

It is well known that nanoparticles with a hydrodynamic diameter of less than 5.5 nm can easily pass through the kidney filtration and have a renal clearance property. These renal-

clearable nanoparticles usually behave like small molecular drugs in both pharmacokinetics and urinary elimination, which thus minimizes their nonspecific accumulation in the RES and potential toxicity.^{22,32–38} In addition, it will significantly improve their biosafety, as these ultrasmall nanoparticles can be renally cleared from the body in their intact form.²² More importantly, these nanoparticles with reasonable sizes and appropriate surface modifications can retain their EPR effect and balance the requirement between clearance efficacy and tumor specificity very well.^{34,39} Inspired by the aforementioned features, herein we present the rational synthesis of ultrasmall MOF QDs *via* a facile method, as well as their usage as renal-clearable nanoagents for enhanced PDT of cancer (Figure 1a). By using a liquid phase exfoliation route, these MOF QDs were prepared from zirconium (Zr)-based porphyrinic NMOFs (PCN-224 NMOFs) with high resistance against complicated physiological conditions.^{15,40} Due to their ultrasmall size and post poly(ethylene glycol) modification (PEGylation), these well-defined MOF QDs exhibit efficient renal clearance and satisfactory cancer accumulation, overcoming the dilemma associated with long-term toxicity.³⁴ Compared with the

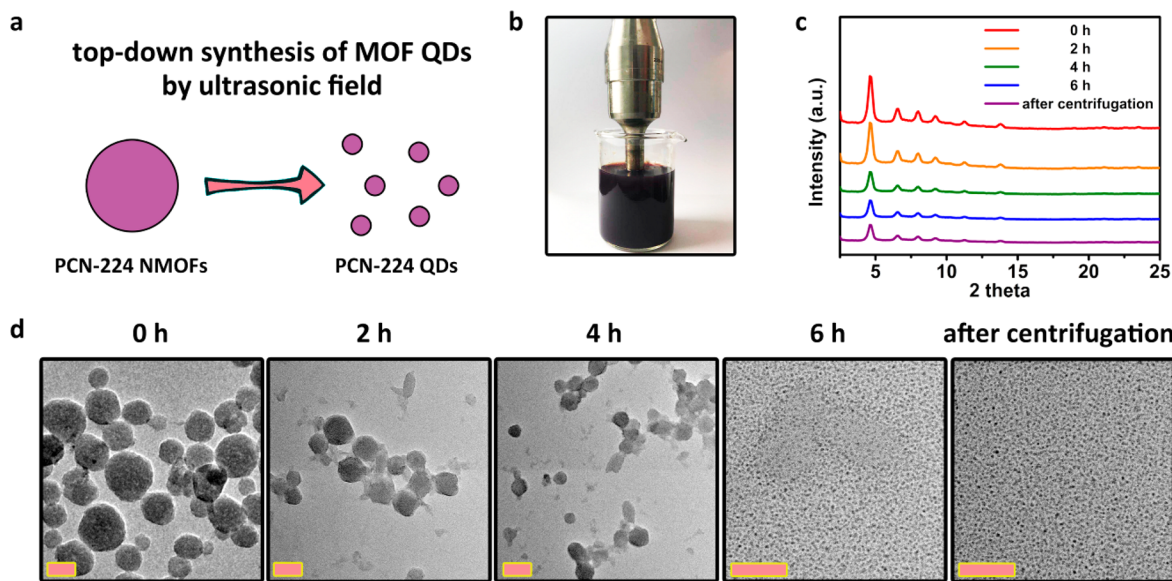


Figure 2. Schematic illustration of the facile top-down synthesis of PCN-224 QDs *via* an ultrasonic route (a) and a photograph of the related ultrasonic route (b). Time-dependent XRD patterns (c) and TEM images (d) of the precursor PCN-224 NMOFs after ultrasonic treatments. Scale bars are equal to 50 nm.

precursor NMOFs and PEGylated PCN-224 NMOFs (PEG-MOFs), these MOF QDs can generate 2-fold effective ROS upon the same light irradiation and provide a better therapeutic efficacy both *in vitro* and *in vivo* because their ultrasmall size can facilitate the diffusion of internally generated ROS out of the frameworks by shortening the distance of ROS diffusion inside the frameworks. All these collective properties of MOF QDs not only highlight their promise as renal-clearable nanoagents for enhanced PDT of cancer but also encourage the further development of ultrasmall MOF-based therapeutic platforms for clinical translation.

RESULTS AND DISCUSSION

Zr-based porphyrinic NMOFs (PCN-224 NMOFs) with a diameter ranging from 50 to 140 nm were first prepared as the precursors according to a classical route (Figure S1, Figure S2a,b).¹⁵ Upon treatment with an ultrasonic processor, a liquid phase exfoliation was introduced to yield PCN-224 nanodots (PCN-224 QDs). As shown in Figure S2c, PCN-224 QDs had a mean diameter of 4.0 nm. Considering the further biorelated usages of these ultrasmall nanoagents, PCN-224 QDs were further modified with poly(ethylene glycol) (PEG) *via* the strong coordination bonds between Zr₆ clusters of PCN-224 QDs and terminal carboxyl groups of carboxylated PEG, which were termed MOF QDs.^{37,41} The sizes of MOF QDs were explored by transmission electron microscope (TEM) imaging, atomic force microscope (AFM) imaging, and dynamic light scattering (DLS) measurement.⁴² TEM images (Figure 1b and Figure S2d) and AFM images (Figure 1c and Figure S3) indicated that these MOF QDs were homogeneous with an average size of 4.0 nm and a topographic average height of 4.0 nm, respectively. Results of DLS measurement demonstrated that these MOF QDs held an average hydrodynamic diameter of 4.5 nm, which was below the renal filtration threshold of 5.5 nm (Figure 1d). Meanwhile, the hydrodynamic diameter of PCN-224 QDs was smaller than that of MOF QDs, indicating the successful surface modification of carboxylated PEG on

PCN-224 QDs. Owing to the larger size of PCN-224 NMOFs, both PCN-224 QDs and MOF QDs had better solubility in water even after 24 h of incubation (Figure S4). Figure 1e additionally demonstrated that these MOF QDs could be well dispersed in water, saline (NaCl, 0.9%), fetal bovine serum (FBS), and Dulbecco's modified Eagle medium (DMEM). X-ray diffraction (XRD) patterns revealed that PCN-224 QDs and MOF QDs had a high degree of consistency with that of pure PCN-224, indicating the retaining of crystallinity during the whole synthetic process (Figure 1f). As shown in Figure S5a, thermogravimetric (TG) curves of PCN-224 NMOFs and PCN-224 QDs were quite similar, which indicated the same architecture of PCN-224 NMOFs and PCN-224 QDs. For the first weight loss step, 14% and 8% weight losses were expected for the solvent within the pores for PCN-224 NMOFs and PCN-224 QDs (30–150 °C). For the second weight loss step, 19% and 20% weight losses were expected for the structural decomposition of PCN-224 NMOFs and PCN-224 QDs (around 490 °C). All these results demonstrated the similar composition of PCN-224 NMOFs and PCN-224 QDs. In addition, TG results shown in Figure S5b indicated that the content of PEG in MOF QDs was about 21 wt % based on the calculated composition. Fourier transform infrared spectroscopy (FT-IR) spectra further demonstrated the presence of carboxylated PEG molecules in MOF QDs (Figure S6). Ultraviolet-visible spectroscopy (UV-vis) absorbance spectra indicated that MOF QDs' chemical structure and related photophysical properties were not affected by the ultrasonic treatment and post-PEGylation (Figure 1g and Figure S7). For further biorelated usages, PEG-NMOFs were then prepared with a similar synthetic process, and related details are shown in the Methods section. Compared with the positive ζ potential values of both PCN-224 NMOFs and PCN-224 QDs, the ζ potential values of PEG-NMOFs and MOF QDs exhibited a significant decrease, demonstrating the successful PEGylation of PCN-224 NMOFs and PCN-224 QDs (Figure S8).¹⁵ All these results indicated that MOF QDs could be synthesized *via* a facile yet efficient route with a relatively high productivity.

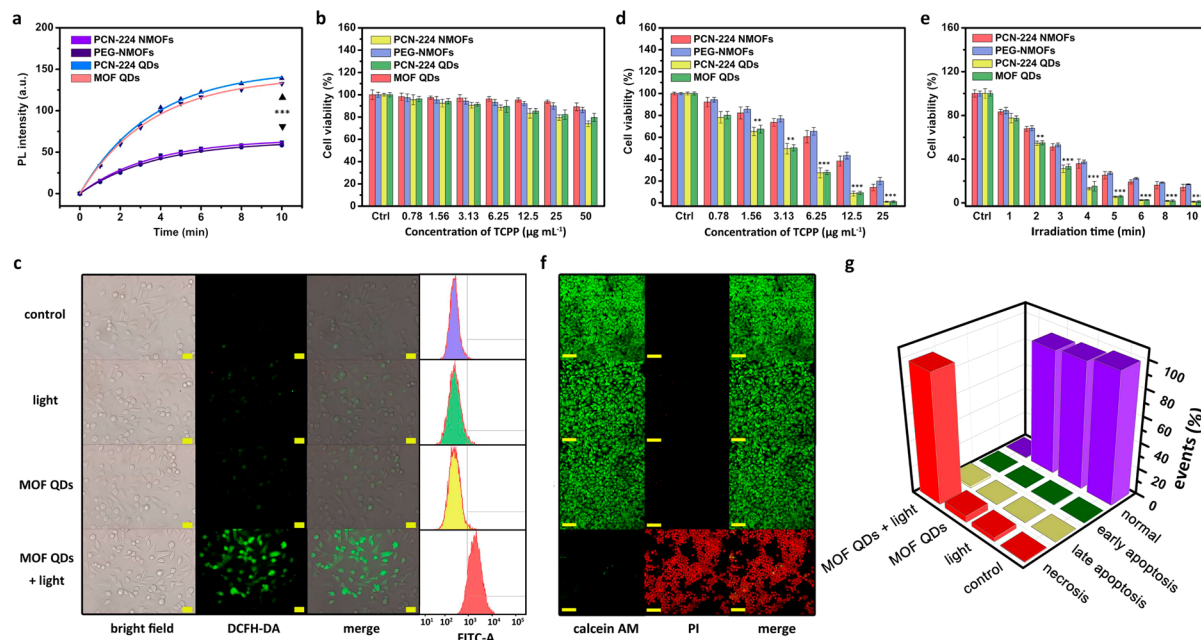


Figure 3. Light-induced ROS generation from PCN-224 NMOFs, PEG-NMOFs, PCN-224 QDs, and MOF QDs upon 650 nm laser irradiation by using DCFH-DA as sensor (a). Cytotoxicity of PCN-224 NMOFs, PEG-NMOFs, PCN-224 QDs, and MOF QDs (b). Cellular images and related flow cytometry analysis of light-induced ROS generation in HeLa cells incubated with MOF QDs upon 650 nm laser irradiation (c). Scale bars are equal to 20 μm . Concentration-dependent (d) and time-dependent (e) PDT efficacy of PCN-224 NMOFs, PEG-NMOFs, PCN-224 QDs, and MOF QDs under 650 nm laser irradiation (d). Fluorescence images of calcein AM and PI costained HeLa cells treated with MOF QDs under 650 nm laser irradiation (f). Scale bars are equal to 100 μm . Apoptosis/necrosis analysis based on flow cytometry upon different treatments (g). Error bars represented standard deviation from the mean ($n = 5$). Asterisks indicate statistically significant differences (* $P < 0.05$, ** $P < 0.01$, *** $P < 0.001$).

In order to investigate the formation process of MOF QDs, a time-dependent ultrasonic experiment was designed and carried out (Figure 2a and b). Compared with the precursors, which were defined as pure PCN-224, all the products retained the same crystallinity even when the ultrasonic period was prolonged to 6 h (Figure 2c). However, the sizes of nanoparticles derived from PCN-224 NMOFs decreased step-by-step along with the increase of the ultrasonic period (Figure 2d). Significantly, after 6 h of ultrasonic treatment, most of the PCN-224 NMOFs could be transformed into PCN-224 QDs. After careful centrifugation, the uniform PCN-224 QDs were separated from the raw products (Figure 2d). Previous studies demonstrated that the presence of defects in MOFs could naturally affect the amount of adsorbed nitrogen and related experimental BET surface.^{43–46} As shown in Figure S9, PCN-224 NMOFs held an experimental BET surface area of 2316.4 m^2/g , which was 34.6% lower than its theoretical value (3530.5 m^2/g) of defect-free PCN-224 crystals, indicating the presence of abundant defective sites in PCN-224 NMOFs. Therefore, the detailed formation process of MOF QDs could be summarized as follows. First, the initial defective sites of PCN-224 NMOFs caused by the locally missed/dislocated ligands and metal ions could significantly decrease the MOF stability.⁴⁶ Second, ultrasonic energy attacked the initial defect sites of PCN-224 NMOFs, and small PCN-224 fragments were generated.^{47,48} Third, newly exposed surface defective sites on PCN-224 fragments could be further attacked upon sonication, and PCN-224 QDs were generated with the increasing of the ultrasonic period.^{49–55} Significantly, ultrasonic energy only broke the defective sites in NMOFs during the preparation; thus the final PCN-224 QDs still retained the same crystallinity of NMOFs. All these

exciting results indicated the rationalization of our design and the successful formation of ultrasmall MOF QDs.

Prior to investigating the PDT efficacy of MOF QDs, we explored the stability of MOF QDs against various physiological solutions including water, saline, and FBS. Chemical structure information (Figure S10) and concentration-dependent UV-vis absorbance spectra (Figure S11a) of the building units of MOF QDs, tetrakis(4-carboxyphenyl)-porphyrin (TCPP), as well as related concentration-absorbance calibration curves (Figure S11b) are provided in detail.³⁹ Results of both UV-vis spectroscopy and inductively coupled plasma optical emission spectrometry (ICP-OES) revealed that all the degradation degrees of MOF QDs in the above physiological solutions were lower than 20% even when the co-incubation period was prolonged to 1 week, indicating the high stability of these MOF QDs (Figure S11c and d). The strong interaction between Zr_6 clusters and carboxylate endowed these MOF QDs with admirable chemical stability.⁴⁰ Then, dichlorodihydrofluorescein diacetate (DCFH-DA) was used as a fluorescent ROS indicator to explore the ROS-generating ability of MOF QDs. The fluorescence intensity was plotted against irradiation time upon 650 nm laser irradiation (Figure 3a). Compared with PCN-224 NMOFs and PEG-NMOFs, PCN-224 QDs and MOF QDs held better ROS-generating abilities upon 650 nm laser irradiation (Figure S12). Considering $^1\text{O}_2$ as the major ROS generated by porphyrinic MOFs, singlet oxygen sensor green (SOSG) was used as a typical $^1\text{O}_2$ indicator to reconfirm our above results. As shown in Figure S13, both PCN-224 QDs and MOF QDs produced more $^1\text{O}_2$ in the presence of light irradiation than those of PCN-224 NMOFs and PEG-NMOFs. Quantitatively, the generation of $^1\text{O}_2$ was depicted with an exponential function

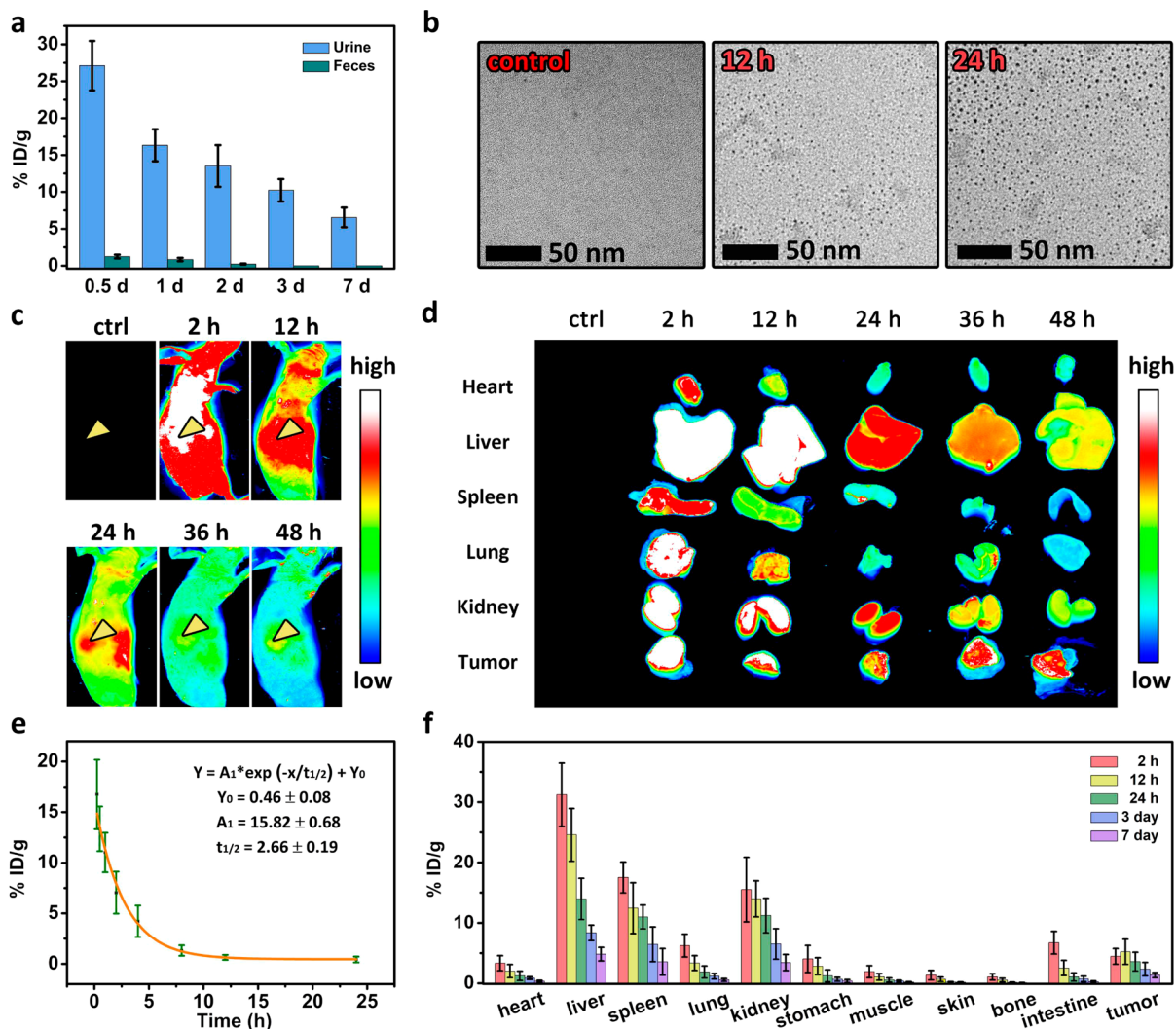


Figure 4. Zr amounts in urine and feces at various intervals from tumor-bearing mice after intravenous injection of MOF QDs (a). TEM images of concentrated urine collected from tumor-bearing mice before and 12 h/24 h after intravenous injection of MOF QDs (b). Time-dependent *in vivo* (c) and *ex vivo* (d) fluorescence imaging of tumor-bearing mice after intravenous injection of Cy5.5-MOF QDs. Pharmacokinetics (e) and biodistribution (f) of MOF QDs from tumor-bearing mice after intravenous injection via ICP-OES. Error bars are equal to one standard deviation from the mean ($n = 5$).

that corresponded to a pseudo-first-order process. The ${}^1\text{O}_2$ generation curve was fitted with the following equation:¹²

$$I_F = A(1 - e^{-kt})$$

I_F is fluorescence intensity and t represents irradiation time, while A and k are fitting parameters (see discussion in *Methods*). The product of Ak in the equation is proportional to the initial rate of the reaction, which indicates the ${}^1\text{O}_2$ -generating efficacy (Table S1). These results demonstrated that PCN-224 QDs and MOF QDs were at least twice as efficient as PCN-224 NMOFs and PEG-NMOFs in generating ${}^1\text{O}_2$ upon the same light irradiation, which was attributed to the better use of ${}^1\text{O}_2$ generated from the interior of PCN-224 QDs and MOF QDs. More importantly, there were negligible differences in the ROS-generating ability between PCN-224 QDs and MOF QDs, indicating that PEGylation did not affect the ROS-generating ability based on our present design.

Encouraged by the outstanding ROS-generating ability of MOF QDs, we further investigated their PDT efficacy *in vitro*. MTT assays associated with HeLa cells without light

irradiation revealed that cellular viabilities were not hindered by MOF QDs, demonstrating the negligible cytotoxicity of these MOF QDs (Figure 3b).^{36–58} Moreover, cellular uptake of MOF QDs was explored. As shown in Figure S14, both MOF QDs and PEG-NMOFs could be effectively internalized by HeLa cells. Although the cellular uptake amounts of MOF QDs were lower than those of PEG-NMOFs under the same incubation periods, there were still enough MOF QD-based photosensitizers internalized by HeLa cells. By using DCFH-DA as a fluorescent sensor, the ROS-generating ability of MOF QDs in HeLa cells upon light irradiation could be visualized by fluorescence microscopy. As shown in Figure 3c, cells in the groups of MOF QDs and light revealed negligible fluorescence, which was similar to that of cells in the control group. However, cells in the group of MOF QDs + light showed intense green fluorescence, suggesting that a large amount of ROS were generated. Results of flow cytometry reconfirmed that MOF QDs could significantly increase the intracellular ROS levels upon light irradiation, indicating that our MOF QDs had an excellent light-induced ROS-generating ability *in vitro*. In addition, *in vitro* PDT efficacy of MOF QDs exhibited

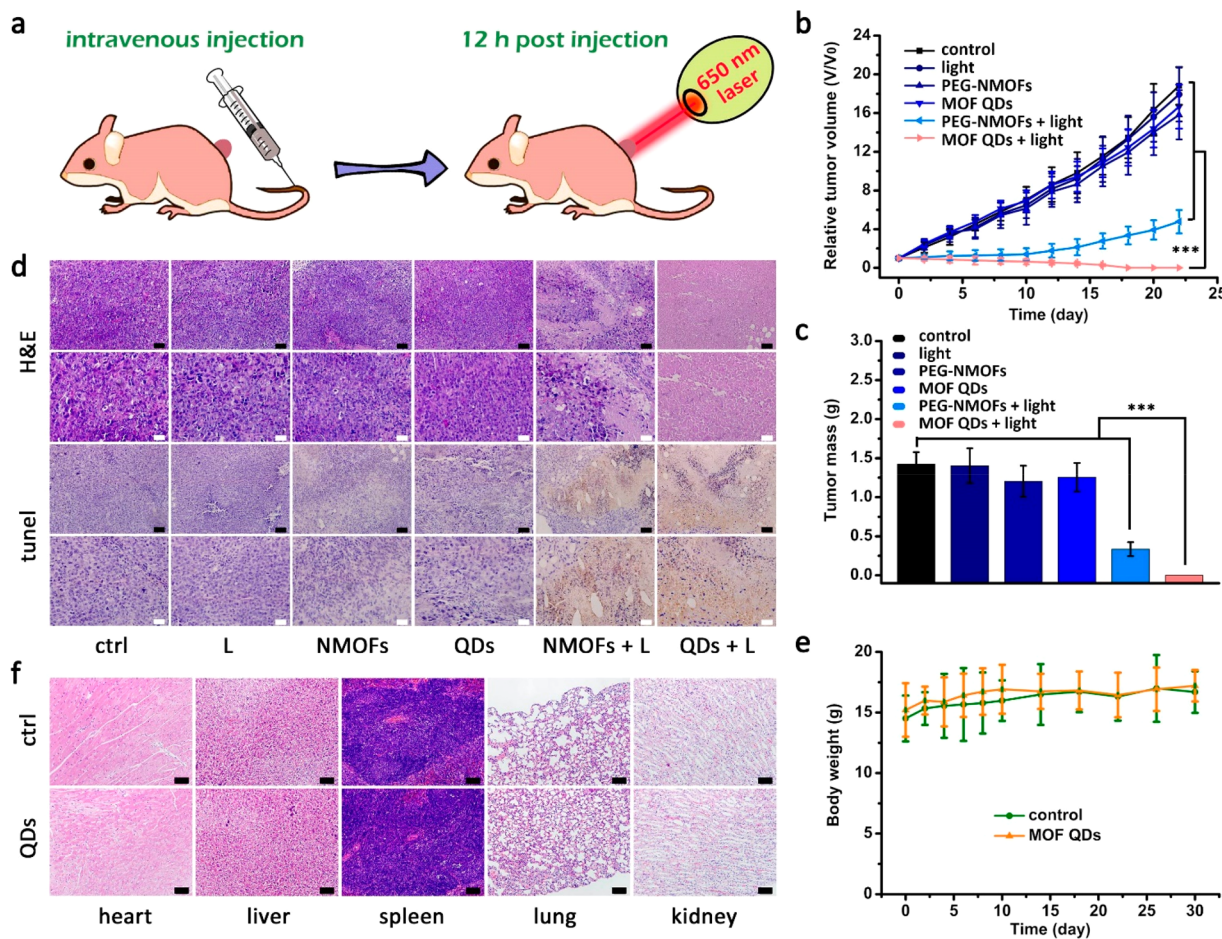


Figure 5. Schematic illustration of the enhanced PDT process (a). Tumor growth curves of the tumor-bearing mice after various treatments (b). Tumor masses collected from the tumor-bearing mice at 3 weeks postinitiation of various treatments (c). H&E/TUNEL-stained images and related enlargements of tumor slices collected from different groups at 14 days postinitiation of various treatments (d). Abbreviations: Ctrl indicates control, L indicates light, NMOFs indicates PEG-NMOFs, and QDs indicates MOF QDs. The black scale bars are equal to 50 μm and the white scale bars are equal to 25 μm . Body-weight change (e) and H&E staining images of major organs (f) of the mice after different treatments. Scale bars are equal to 50 μm . Error bars represent standard deviation from the mean ($n = 5$). Asterisks indicate statistically significant differences (* $P < 0.05$, ** $P < 0.01$, *** $P < 0.001$).

a concentration-dependent manner and an irradiation period-dependent manner (Figure 3d and e). When the light irradiation intensity and period were defined as 1 W cm^{-2} and 10 min in the typical experiment, the PDT IC₅₀ values of PCN-224 NMOFs, PEG-NMOFs, PCN-224 QDs, and MOF QDs could be calculated as 8.43, 10.32, 3.01, and 3.13 $\mu\text{g mL}^{-1}$, respectively. Owing to the similar structure of PCN-224 QDs and MOF QDs, their IC₅₀ values were almost the same. However, the IC₅₀ value of PCN-224 NMOFs and PEG-NMOFs was much higher than those of PCN-224 QDs and MOF QDs due to the limited ROS diffusion distance (10 nm) and the relatively large sizes of PCN-224 NMOFs and PEG-NMOFs. Results of the live-dead cell staining verified the admirable PDT efficacy of MOF QDs (Figure 3f). Analysis based on flow cytometry further revealed that nearly all the cells were killed in the presence of MOF QDs upon light irradiation via an apoptosis process (Figure 3g and Figure S15).⁵⁹ All these results demonstrated that our well-prepared MOF QDs exhibited obvious photoinduced cytotoxicity, which could be attributed to the effective use of the internally generated ROS of MOF QDs.

Compared with the size threshold for efficient renal filtration of 5.5 nm, our well-developed MOF QDs were much smaller,

which could prevent the potential long-term retention and toxicity. Accordingly, we further explored the clearance route and biodistribution of these MOF QDs in detail. First, MOF QDs were intravenously injected into tumor-bearing mice. Second, samples including urine, feces, and blood were collected and tested. Time-dependent ICP-OES analysis of the Zr amounts revealed that most of the injected MOF QDs could be found in the urine within 1 week, while only a small amount was eliminated via the feces, demonstrating that MOF QDs were excreted from the mouse bodies mainly through the renal pathway (Figure 4a). As shown in Figure 4b, MOF QDs could be found in the TEM images of urine samples collected at both 12 and 24 h postinjection (p.i.), indicating that these MOF QDs with high stability against complicated physiological conditions could be excreted in their intact form. Time-dependent *in vivo* and *ex vivo* fluorescence imaging was then carried out to monitor the biodistribution of MOF QDs visually. Compared with TCPP, MOF QDs had weaker fluorescence with the same TCPP concentration based on some recent studies including ours (Figure S16a).⁴¹ These decreases of fluorescence intensity might stem from the enhanced intersystem crossing (ISC) after coordinating the porphyrin ligands to heavy metal clusters, which was highly

consistent with other porphyrinic MOF systems.¹⁴ However, the above enhanced ISC transition of the photosensitizer could extremely improve the $^1\text{O}_2$ yield and enhance the PDT efficacy, which were more suitable for future therapy systems.²¹ The excitation wavelength of both TCPP and MOF QDs was around 420 nm, which had low penetration capacity and was not suitable for bioimaging. Thus, Cy5.5-MOF QDs with an excitation wavelength of 680 nm were rationally designed and prepared first. As shown in Figure S16b, Cy5.5-MOF QDs revealed an excellent fluorescence property with an emission wavelength around 700 nm. As shown in Figure 4c and d, Cy5.5-MOF QDs could be easily detected in various exposed organs and tumors within the first 12 h after intravenous injection, which indicated their relatively long blood circulation time and satisfactory tumor accumulation. With the time passing, fluorescent signals from Cy5.5-MOF QDs in various organs decreased sharply, whereas fluorescent signals in tumors altered slightly. These results well demonstrated the efficient renal clearance of MOF QDs and their high enhanced permeability and retention (EPR) effect in tumors. The blood circulation half-life of MOF QDs could be determined as 2.66 ± 0.19 h, which was slightly shorter than that of PEG-NMOFs (3.97 ± 0.57 h), further indicating that MOF QDs with reasonable size and post-PEGylation could lead to a relative long blood circulation time (Figure 4e and Figure S17). According to the quantitative analysis of biodistribution shown in Figure 4f, MOF QDs revealed high accumulation in tumors and the tumor accumulation reached the peak level of 5.21% ID/g 12 h after intravenous injection. Moreover, most of the MOF QDs still remained in the kidneys 24 h after intravenous injection, and the levels of Zr in other organs significantly decreased over time. By contrast, PEG-NMOFs exhibited high accumulation in the liver and spleen even at 7 days after intravenous injection, and negligible kidney accumulation was detected during the whole experimental period (Figure S18). The above biodistribution differences between MOF QDs and PEG-NMOFs indicated that the main clearance pathway of the ultrasmall MOF QDs was through a renal manner. All the above results strongly evidenced the efficient renal clearance of MOF QDs and their potential for further *in vivo* PDT of cancer.

Figure 5a schematically illustrates the MOF QD-based PDT of cancer and tumor-bearing mice used to explore the *in vivo* antitumor efficacy of these MOF QDs upon light irradiation. Mice were randomly divided into six groups and defined as control, light alone, MOF QDs alone, MOF QDs + light, PEG-NMOFs alone, and PEG-NMOFs + light, respectively. Tumor volumes and weights were measured to explore the antitumor efficacy of MOF QDs upon light irradiation. As shown in Figure 5b and c, mice treated with MOF QDs alone, PEG-NMOFs alone, and light alone showed no obvious effect on the tumor growth as compared with the control group. By contrast, groups including MOF QDs + light and PEG-NMOFs + light held obvious suppressive effects on tumor growth. More importantly, complete tumor elimination occurred in the group of MOF QDs + light at 18 days postinitiation of the treatment, and no tumor relapse was observed in further days, indicating a more significant tumor growth-inhibition effect compared with PEG-NMOFs + light. In order to obtain accurate and intact staining information on tumors, 14 days was selected as the experimental terminal point to perform H&E staining and TUNEL staining for further exploration of therapeutic efficacy.⁶⁰ As expected, the

group of MOF QDs + light had the highest level of tumor cell apoptosis among all the experimental groups (Figure 5d). Moreover, mice in the groups of MOF QDs + light significantly prolonged survival lifetime compared to other groups (Figure S19). According to the above results, MOF QDs possessed an admirable PDT efficacy for cancer therapy. Given their excellent therapeutic efficacy, we then investigated the long-term toxicity of these MOF QDs in healthy mice after intravenous injection.⁶¹ Compared with the control group, mice in the test group showed negligible differences in body weight, eating, drinking, and activity during the whole experimental period (Figure 5e). A hemolytic assay was carried out to explore the interaction between our MOF QDs and blood components. No hemolysis could be found after the co-incubation with MOF QDs (Figure S20). H&E staining images of major exposed organs from mice after different treatments indicated that MOF QDs possessed high biocompatibility and negligible systemic toxicity (Figure 5f). To provide a quantitative assessment of long-term toxicity, results of blood biochemistry and hematology revealed that there were no significant differences between the test group and the control group, and all the parameters fell in the reference index (Figure S21). All these results suggested the overall safety of our MOF QDs and their promising potential for further practical therapeutic usage.

CONCLUSIONS

In summary, we rationally designed and synthesized ultrasmall MOF QDs *via* a facile yet efficient approach and utilized them as high-performance renal-clearable nanoagents for the enhanced PDT of cancer. These MOF QDs with well-defined crystal structure possessed efficient renal clearance and sufficient tumor accumulation, which could extremely overcome the long-term toxicity induced by the undefined residue after systemic administration. Compared with NMOFs and PEG-NMOF, our MOF QDs can generate 2-fold effective ROS upon the same light irradiation conditions and greatly decrease the inefficacy of the PDT caused by the inefficient use of ROS generated from the interior of NMOFs and PEG-NMOFs. Moreover, long-term toxicity after intravenous injection of these MOF QDs indicated their extremely low systemic toxicity and overall safety. We believe that this study not only facilitates the utilization of ultrasmall renal-clearable MOF QDs for nontoxic and efficient cancer therapy but also encourages the development of versatile MOF-based nano-platforms for further biomedical utility.

METHODS

Chemicals. Tetrakis(4-carboxyphenyl)porphyrin and benzoic acid (BA) were purchased from TCI. Zirconyl chloride octahydrate ($\text{ZrOCl}_2 \cdot 8\text{H}_2\text{O}$), DCFH-DA, calcein AM, and propidium iodide (PI) were purchased from Sigma-Aldrich. HOOC-PEG-COOH ($M_w = 1000$) and Cy5.5-PEG-COOH ($M_w = 1000$) were purchased from ToYong Biotechnology. *N,N*-Dimethylformamide (DMF) was purchased from Aladdin. Singlet oxygen sensor green reagent was purchased from Thermo Fisher Scientific. Ltd. Ultrapure water was prepared *via* a Milli-Q-Plus water system ($18.2 \text{ M}\Omega \text{ cm}^{-1}$) and used in all the experiments. Dialysis bags (molecular weight cut off: 3.5 kDa) were ordered from Spectrumlabs (USA). Other reagents were of analytical grade and used as received.

Synthesis of PCN-224 NMOFs. TCPP (100 mg), $\text{ZrOCl}_2 \cdot 8\text{H}_2\text{O}$ (300 mg), and BA (2.8 g) were dissolved in DMF (100 mL), and the mixture was stirred at 90°C . Five hours later, PCN-224 NMOFs were

collected by centrifugation (18 000 rpm, 30 min), washed with DMF, and redispersed in DMF for further use.

Synthesis of PEG-NMOFs. PCN-224 NMOFs (10 mg) were mixed with excess HOOC-PEG-COOH (50 mg) in ultrapure water under stirring at room temperature. Thirty minutes later, the obtained PEG-NMOFs were collected by centrifugation and freeze-dried for further use.

Synthesis of PCN-224 QDs. First, PCN-224 NMOFs (100 mg) were dissolved in ultrapure water (100 mL) at room temperature. Second, the obtained suspension was treated with an ultrasonic processor at a power of 200 W. After centrifugation (12 000 rpm, 20 min), PCN-224 QDs were collected in supernatant, washed with ultrapure water *via* dialysis, and lyophilized for further use.

Synthesis of MOF QDs. PCN-224 QDs (10 mg) in ultrapure water (10 mL) were mixed with HOOC-PEG-COOH (50 mg) under stirring at room temperature. Thirty minutes later, the above solution was purified *via* dialysis and lyophilized to result in MOF QDs.

Synthesis of Cy5.5-MOF QDs. PCN-224 QDs (1 mg) were mixed with Cy5.5-PEG-COOH (5 mg) in ultrapure water (1 mL) under stirring at room temperature. Thirty minutes later, the above solution was purified *via* dialysis and lyophilized to result in Cy5.5-MOF QDs.

Characterization. TEM and HR-TEM images were recorded on a FEITECNAI G220 high-resolution transmission electron microscope. Crystalline structures of samples were evaluated on a Rigaku-Dmax 2500 diffractometer. UV-vis absorbance measurements were carried out on a JASCO V-550 UV-vis spectrophotometer. Fluorescence measurements were carried out on a Jasco FP-6500 spectrofluorometer. ζ potential measurements were carried out on a Malvern Nano ZS-90. Quantitative analysis of the Zr content was obtained by ICP-OES (Agilent 7700x series). FT-IR was obtained on a Bruker Vertex 70 FT-IR spectrometer; 32 scans were taken with a spectral resolution of 2 cm^{-1} . The nitrogen sorption isotherm was measured using a Micrometrics ASAP 2420 system with high-purity grade of gases at 77 K.

N_2 Adsorption–Desorption Measurement of PCN-224 NMOFs. Before measurement, PCN-224 NMOFs were washed with DMF three times and acetone three times, respectively. Then, PCN-224 NMOFs were dried in a preheated 85 °C oven for more than 30 min. Finally, the resulting purple powder was activated on ASAP 2020 for N_2 adsorption measurement at 150 °C for 5 h.

TG Analysis. For TG analysis, 10 mg of PCN-224 NMOFs, PCN-224 QDs, or MOF QDs was heated on a TGA-50 (Shimadzu) thermogravimetric system from room temperature to 800 °C at a rate of $10\text{ }^{\circ}\text{C min}^{-1}$ under a N_2 flow of 50 mL min^{-1} .

Theoretical Surface Area of PCN-224. The theoretical surface area of PCN-224 was calculated by an Atom Volume & Surface calculation using the Materials Studio 8 software package with a solvent radius of 3.64 \AA (N_2). The occupied volume, the free volume, and the surface area could be calculated as 11006.22 \AA^3 , 45904.91 \AA^3 , and 10227.07 \AA^2 , respectively. Thus, theoretical surface area (m^2) = surface area (\AA^2) / [density (g/cm^3) \times cell volume (\AA^3) / 10^4], where cell volume (\AA^3) = occupied volume (\AA^3) + free volume (\AA^3). Thus, the theoretical density of defect-free PCN-224 was 0.509 g/m^3 .

Quantitative Analysis of MOF QDs' Degradation. Standard solutions of TCPP were prepared in a mixture of H_2O and DMF with a volume ratio of 1:1. UV-vis spectra of TCPP standard solutions with various concentrations were measured. A calibration curve based on the absorbance at 416 nm and the concentration of TCPP was plotted. MOF QDs with a TCPP concentration of $25\text{ }\mu\text{g mL}^{-1}$ dispersed in FBS, saline, or ultrapure water were then dialyzed against these solutions, respectively. Related medium was taken out and measured on a Jasco-V550 UV-vis spectrophotometer. Moreover, the amounts of Zr released from MOF QDs were quantified *via* ICP-OES.

ROS-Generating Ability of MOF QDs. DCFH-DA was used to explore the ROS-generating ability of MOF QDs. MOF QDs with a TCPP concentration of $25\text{ }\mu\text{g mL}^{-1}$ were mixed with DCFH-DA (10 μM), and the solution was irradiated under a 650 nm laser (1 W cm^{-2}). After irradiation, fluorescence intensity at 525 nm was measured to explore the ROS-generating ability (Ex: 488 nm).

${}^1\text{O}_2$ -Generating Ability of MOF QDs. SOSG was used as a fluorescent probe to investigate the ${}^1\text{O}_2$ -generating ability of MOF QDs. In brief, SOSG (100 μg) was dissolved in DMSO (330 μL) to obtain an SOSG stock solution (0.5 mM). Then, MOF QDs with a TCPP concentration of $25\text{ }\mu\text{g mL}^{-1}$ were mixed with SOSG (10 μM), and the solution was irradiated under a 650 nm laser (1 W cm^{-2}). In the presence of ${}^1\text{O}_2$, SOSG exhibited a green fluorescence around 525 nm (Ex: 504 nm).

${}^1\text{O}_2$ -Generating Efficacy of MOF QDs. ${}^1\text{O}_2$ generation curves were fitted with the following equation. As the light intensity and photosensitizer concentration were fixed, for the photoreaction, we could assume that $[\text{PS}^*]$ (the concentration of the excited state of the photosensitizer) was a constant. Therefore, we provided the ${}^1\text{O}_2$ -generating rate equation:

$$\frac{d[{}^1\text{O}_2]}{dt} = -d[\text{O}_2]/dt = k[\text{PS}^*][\text{O}_2] = k^*[\text{O}_2]$$

where $k^* = k[\text{PS}^*]$. A coupled reaction of SOSG to consume ${}^1\text{O}_2$ is

$$\frac{d[\text{SOSG}^*]}{dt} = k_2[{}^1\text{O}_2][\text{SOSG}]$$

where $[\text{SOSG}^*]$ is the concentration of the SOSG reacted form.

Applying a steady state assumption on $[{}^1\text{O}_2]$,

$$\frac{d[{}^1\text{O}_2]}{dt} = k^*[\text{O}_2] - k_d[{}^1\text{O}_2] - k_2[{}^1\text{O}_2][\text{SOSG}] = 0$$

$$[{}^1\text{O}_2] = k^*[\text{O}_2]/k_d + k_2[\text{SOSG}]$$

where k_d is the rate constant of ${}^1\text{O}_2$ loss (relaxation or quenched by other species in the solution). When $k_2[\text{SOSG}] \ll k_d$ and $[\text{O}_2]$ is high,

$$[{}^1\text{O}_2] \approx k^*[\text{O}_2]/k_d = \text{constant}$$

$$dI_F/dt \text{ was proportional to } d[\text{SOSG}^*]/dt = k_1[\text{SOSG}]$$

where $k_1 = k_2k^*[\text{O}_2]/k_d$ and I_F was proportional to $[\text{SOSG}^*]$:

$$I_F = I_0\varphi_f\varepsilon_S b[\text{SOSG}^*]$$

where I_0 is the incident light intensity, φ_f is the fluorescence quantum yield of SOSG^* , ε_S is the extinction coefficient of SOSG^* , and b is the light path length. We could integrate the equation to obtain the correlation of fluorescence intensity I_F and irradiation time t :

$$\ln([\text{SOSG}]/c_0) = -k_1 t$$

$$I_F = A[1 - e^{-kt}]$$

where c_0 is the initial concentration of SOSG and A and k are different fitting parameters. Thus,

$$A = \varphi_f I_0 \varepsilon_S b c_0$$

$$k = \varphi_\Delta N_{ir} \varepsilon_{ps} b c k_2 / k_d$$

where φ_Δ is the quantum yield of ${}^1\text{O}_2$ generation, N_{ir} is the irradiation light intensity by photons per second, ε_{ps} is the extinction coefficient of PS at the emission wavelength, and c is the concentration of PS. Linear approximations were used in the above equations. By nonlinear regression, we obtained a series of fit curves with the aforementioned function.

Then, by deriving the equation $I_F = A[1 - e^{-kt}]$, we obtained

$$I_F/dt = A k e^{-kt}$$

$$\text{when } t \rightarrow 0, dI_F/dt = Ak$$

Thus, the product of Ak in the equation was proportional to the initial rate of the reaction that indicated the efficacies of ${}^1\text{O}_2$ generation. Results based on all fitting parameters are provided in Table S1.

Cell Culture. HeLa cells were cultured at 37 °C under 5% CO_2 . Media was DMEM containing FBS (10%), penicillin (100 U mL^{-1}), and streptomycin (100 mg mL^{-1}), which was changed every other day. Cells were digested by trypsin and resuspended in fresh media before plating.

MTT Assay. HeLa cells were seeded in a 96-well plate with a density of 10^4 per well for 12 h. MOF QDs with different concentrations were added into the medium. Twenty-four hours later, cells were treated with MTT for another 4 h. DMSO was added to dissolve the formazan crystals, and a Bio-Rad model-680 microplate reader was used to measure the absorbance at 490 nm with λ 70 nm as a reference.

Cellular Uptake. HeLa cells were seeded in a six-well plate with a density of 10^5 per well. Twenty-four hours later, cells were treated with MOF QDs ($25 \mu\text{g mL}^{-1}$ of TCPP) for different periods. Then, cells were washed with a 0.9% NaCl solution and trypsinized. After centrifugation, cells were washed, resuspended, and counted. Later, cells were dissolved in *aqua regia* at 80°C for 2 h, and Zr amounts in the above samples were assessed via ICP-OES.

In Vitro ROS-Generating Ability of MOF QDs. HeLa cells were seeded in a six-well plate with a density of 10^5 per well for 12 h. MOF QDs with a TCPP concentration of $25 \mu\text{g mL}^{-1}$ were added and incubated for another 4 h. Then, cells were washed with saline and incubated with DCFH-DA ($10 \mu\text{M}$). Twenty minutes later, cells were irradiated with a 650 nm laser (1 W cm^{-2}) for 10 min. ROS fluorescence intensity of cells was monitored via flow cytometry and fluorescence microscopy.

In Vitro PDT Efficacy. For *in vitro* PDT, HeLa cells were seeded in a 96-well plate with a density of 10^4 per well for 12 h. MOF QDs with a TCPP concentration of $25 \mu\text{g mL}^{-1}$ were added and incubated for another 4 h. After cells were irradiated with a 650 nm laser (1 W cm^{-2}) for 10 min, cells were incubated for another 24 h. *In vitro* PDT efficacy was evaluated by the MTT assay. Apoptosis amounts were determined by using an annexin V-FITC apoptosis detection kit. Briefly, cells were first treated with MOF QDs with a TCPP concentration of $25 \mu\text{g mL}^{-1}$ in the presence or absence of 650 nm laser irradiation (1 W cm^{-2} , 10 min). Then, cells were treated by trypsinization, washed with saline, resuspended in annexin V binding buffer, incubated with annexin V and PI at room temperature for 15 min in the dark, and subjected to flow cytometry.

Cellular Modality and Viability Observation. HeLa cells were cultured in a six-well plate with a density of 10^5 per well for 6 h to allow the attachment of cells. After cells were washed by saline, MOF QDs with a TCPP concentration of $25 \mu\text{g mL}^{-1}$ were added to the above medium. Six hours later, cells were irradiated with a 650 nm laser (1 W cm^{-2}) for 10 min, and treated cells were placed in an incubator for further incubation. Twenty-four hours later, staining based on calcein AM and PI was used to confirm the visualized viability of cells.

Animal and Tumor-Bearing Mouse Model. All animal experiments were performed in accordance with the NIH guidelines for the care and use of laboratory animals (NIH Publication No. 85-23 Rev. 1985) and approved by the Jilin University Animal Care and Use Committee. Balb/c nude mice (8–10 weeks, 15 g) were obtained from Laboratory Animal Centre of Jilin University (Changchun, China), and all animal care and handling procedures were in accordance with the guidelines approved by the ethics committee of Jilin University. The tumor-bearing mouse model was established first. HeLa cells were suspended in saline and subcutaneously injected on the back of mice. Then, tumor volume was calculated as $(\text{tumor length}) \times (\text{tumor width})^2 \times 0.5$.

Renal Clearance Analysis. Tumor-bearing mice were intravenously injected with MOF QDs with a TCPP concentration of 5 mg kg^{-1} . Afterward, urine and feces were collected at different time points. Samples were dissolved in *aqua regia* at 80°C for 2 h, and the Zr amounts were measured via ICP-OES. TEM imaging was used to explore the urine samples.

Pharmacokinetics. To explore the pharmacokinetics of MOF QDs and PEG-NMOFs, tumor-bearing mice were intravenously injected with MOF QDs or PEG-NMOFs with a TCPP concentration of 5 mg kg^{-1} . Afterward, blood was collected at different time points. Samples were incubated with *aqua regia* at 80°C for 2 h, and the Zr amounts were measured via ICP-OES.

Biodistribution Analysis. Tumor-bearing mice were intravenously injected with MOF QDs or PEG-NMOFs with a TCPP

concentration of 5 mg kg^{-1} and sacrificed at different time points. Tumors and major organs were harvested for the quantitative analysis of the biodistribution of MOF QDs or PEG-NMOFs. Typically, tumors and major organs were surgically removed from the mice and dissolved in *aqua regia*. The mixtures were heated at 80°C for 2 h, and the Zr amounts in the above samples were assessed via ICP-OES.

Fluorescence Imaging of MOF QDs. Mice were intravenously injected with MOF QDs with a TCPP concentration of 5 mg kg^{-1} (0.74 mg kg^{-1} Cy5.5). Afterward, mice were imaged at various specific times by using IVIS Spectrum 200. Then, mice were sacrificed and major organs and tumors were collected and imaged at various expected time points. Related images were analyzed using ImageJ Software.

In Vivo PDT Efficacy. Tumor-bearing mice were randomly divided into six groups and defined as control, light, MOF QDs, PEG-NMOFs, PEG-NMOFs + light, and MOF QDs + light, respectively. Then, mice were intravenously injected with MOF QDs or PEG-NMOFs with a TCPP concentration of 5 mg kg^{-1} twice a week. The groups of light, MOF QDs + light, and PEG-NMOFs + light received a 650 nm laser irradiation (1 W cm^{-2} , 10 min) at 12 h after intravenous injection. Tumor sizes were measured by using calipers after various treatments. Tumor sizes were recorded for 3 weeks. Then, mice were sacrificed and tumors were collected for tumor mass measurement.

Histological Analysis. Tumor-bearing mice were randomly divided into six groups and defined as control, light, MOF QDs, PEG-NMOFs, PEG-NMOFs + light, and MOF QDs + light, respectively. Then, the mice were intravenously injected with MOF QDs or PEG-NMOFs with a TCPP concentration of 5 mg kg^{-1} twice a week. The groups of light, MOF QDs + light, and PEG-NMOFs + light received 650 nm laser irradiation (1 W cm^{-2} , 10 min) at 12 h after intravenous injection. Fourteen days later, mice were sacrificed, and major tissues including tumors, heart, liver, spleen, lung, and kidney were harvested and fixed with paraformaldehyde (4%), dehydrated, embedded in paraffin, sectioned, and stained with H&E. Slides were observed on an Olympus BX-51 optical system.

Immunohistochemical Staining. Harvested tumors were fixed with paraformaldehyde (4%), dehydrated, embedded in paraffin, sectioned, treated with TUNEL (colorimetric TUNEL apoptosis assay kit, Beyotime), and observed on an Olympus BX-51 optical system.

Survival Rate Analysis. Tumor-bearing mice were randomly divided into four groups and defined as control, light, MOF QDs, and MOF QDs + light, respectively. Mice with a tumor greater than 20 mm in any one dimension were euthanized and considered to be dead for the purpose of drawing the survival curves. The survival rates of mice were recorded for 60 days.

Body Weight Measurement. For body weight measurements, mice were separated into two groups. MOF QDs with a TCPP concentration of 5 mg kg^{-1} were intravenously injected into the mice, which were defined as the test. Mice without any treatment were defined as the control. Related mouse body weight was recorded for 30 days.

Hemolysis Assay. Human blood samples stabilized by EDTA (1 mL) were added to a saline solution (2 mL), and red blood cells were collected by centrifugation. The above samples were washed with saline, and purified red blood cells were diluted to 1/10 of their volume with saline. The diluted suspension (0.2 mL) was mixed with saline (0.8 mL) as a negative control, ultrapure water (0.8 mL) as a positive control, and MOF QD suspensions (0.8 mL) as experimental groups. All the mixtures were vortexed and kept at room temperature for another 3 h. Then, the above mixtures were centrifuged, and the absorbance of the supernatants at 541 nm was determined by UV-vis spectroscopy. Hemolysis was calculated as follows: hemolysis percentage = $[(\text{Abs}_{\text{sample}} - \text{Abs}_{\text{negative control}})/(\text{Abs}_{\text{positive control}} - \text{Abs}_{\text{negative control}})] \times 100\%$.

Hematology Analysis and Blood Biochemical Assay. Blood of mice treated with MOF QDs with a TCPP concentration of 5 mg kg^{-1} were collected at each expected time point after intravenous injection, and the samples were used to carry out the hematological

analysis and blood biochemical assay. Blood from the mice without any treatments was defined as the control.

Statistical Analysis. All data were expressed as mean \pm standard deviation (SD) and performed in 5 specimens. A *P*-value < 0.05 was considered statistically significant. Statistical analysis was performed using one-way analysis of variance (ANOVA) followed by a *post hoc* LSD test.

ASSOCIATED CONTENT

Supporting Information

The Supporting Information is available free of charge on the ACS Publications website at DOI: [10.1021/acsnano.9b03531](https://doi.org/10.1021/acsnano.9b03531).

Experimental details and supporting figures including SEM images, TEM images, height profiles, time-dependent digital photos, TG analysis, FT-IR spectra, UV-vis spectra, ζ potential measurements, photoluminescence spectrum, N₂adsorption-desorption isotherms, stability exploration, fluorescence experiments, cellular uptake, flow cytometry analysis, biodistribution, pharmacokinetics, survival curves, hemolysis results, blood biochemistry, and hematology ([PDF](#))

AUTHOR INFORMATION

Corresponding Authors

*E-mail: liuganxuan@mail.buct.edu.cn.
*E-mail: jren@ciac.ac.cn.
*E-mail: xqu@ciac.ac.cn.

ORCID

Jinsong Ren: [0000-0002-7506-627X](#)

Xiaogang Qu: [0000-0003-2868-3205](#)

Author Contributions

#H.W. and D.Y. contributed equally to this work.

Notes

The authors declare no competing financial interest.

ACKNOWLEDGMENTS

Financial support was provided by National Natural Science Foundation of China (21431007, 21533008, 21871249, 91856205, and 21820102009), Key Research Program of Frontier Sciences of CAS (QYZDY-SSW-SLH052), and Jilin Province Science and Technology Development Plan Project (20170101184JC).

REFERENCES

- (1) Zhou, H. C. J.; Kitagawa, S. Metal-Organic Frameworks (MOFs). *Chem. Soc. Rev.* **2014**, *43*, 5415–5418.
- (2) Denny, M. S., Jr.; Moreton, J. C.; Benz, L.; Cohen, S. M. Metal-Organic Frameworks for Membrane-Based Separations. *Nat. Rev. Mater.* **2016**, *1*, 16078.
- (3) Huang, Y. B.; Liang, J.; Wang, X. S.; Cao, R. Multifunctional Metal-Organic Framework Catalysts: Synergistic Catalysis and Tandem Reactions. *Chem. Soc. Rev.* **2017**, *46*, 126–157.
- (4) Stassen, I.; Burtch, N.; Talin, A.; Falcaro, P.; Allendorf, M.; Ameloot, R. An Updated Roadmap for the Integration of Metal-Organic Frameworks with Electronic Devices and Chemical Sensors. *Chem. Soc. Rev.* **2017**, *46*, 3185–3241.
- (5) Trickett, C. A.; Helal, A.; Al-Maythalony, B. A.; Yamani, Z. H.; Cordova, K. E.; Yaghi, O. M. The Chemistry of Metal-Organic Frameworks for CO₂ Capture, Regeneration and Conversion. *Nat. Rev. Mater.* **2017**, *2*, 17045.
- (6) Zhang, K.; Yu, Z.; Meng, X.; Zhao, W.; Shi, Z.; Yang, Z.; Dong, H.; Zhang, X. A Bacteriochlorin-Based Metal-Organic Framework Nanosheet Superoxide Radical Generator for Photoacoustic Imaging-Guided Highly Efficient Photodynamic Therapy. *Adv. Sci.* **2019**, *1900530*.
- (7) He, C.; Lu, K.; Liu, D.; Lin, W. Nanoscale Metal-Organic Frameworks for the Co-Delivery of Cisplatin and Pooled siRNAs to Enhance Therapeutic Efficacy in Drug-Resistant Ovarian Cancer Cells. *J. Am. Chem. Soc.* **2014**, *136*, 5181–5184.
- (8) He, C.; Liu, D.; Lin, W. Nanomedicine Applications of Hybrid Nanomaterials Built from Metal-Ligand Coordination Bonds: Nanoscale Metal-Organic Frameworks and Nanoscale Coordination Polymers. *Chem. Rev.* **2015**, *115*, 11079–11108.
- (9) Zhang, S. Y.; Shi, W.; Cheng, P.; Zaworotko, M. J. A Mixed-Crystal Lanthanide Zeolite-Like Metal-Organic Framework as a Fluorescent Indicator for Lysophosphatidic Acid, a Cancer Biomarker. *J. Am. Chem. Soc.* **2015**, *137*, 12203–12206.
- (10) Zheng, H.; Zhang, Y.; Liu, L.; Wan, W.; Guo, P.; Nyström, A. M.; Zou, X. One-Pot Synthesis of Metal-Organic Frameworks with Encapsulated Target Molecules and Their Applications for Controlled Drug Delivery. *J. Am. Chem. Soc.* **2016**, *138*, 962–968.
- (11) Wu, M.-X.; Yang, Y. W. Metal-Organic Framework (MOF)-Based Drug/Cargo Delivery and Cancer Therapy. *Adv. Mater.* **2017**, *29*, 1606134.
- (12) Lu, K.; He, C.; Lin, W. Nanoscale Metal-Organic Framework for Highly Effective Photodynamic Therapy of Resistant Head and Neck Cancer. *J. Am. Chem. Soc.* **2014**, *136*, 16712–16715.
- (13) Lu, K.; He, C.; Lin, W. A Chlorin-Based Nanoscale Metal-Organic Framework for Photodynamic Therapy of Colon Cancers. *J. Am. Chem. Soc.* **2015**, *137*, 7600–7603.
- (14) Lu, K.; He, C.; Guo, N.; Chan, C.; Ni, K.; Weichselbaum, R. R.; Lin, W. Chlorin-Based Nanoscale Metal-Organic Framework Systemically Rejects Colorectal Cancers via Synergistic Photodynamic Therapy and Checkpoint Blockade Immunotherapy. *J. Am. Chem. Soc.* **2016**, *138*, 12502–12510.
- (15) Park, J.; Jiang, Q.; Feng, D.; Mao, L.; Zhou, H. C. Size-Controlled Synthesis of Porphyrinic Metal-Organic Framework and Functionalization for Targeted Photodynamic Therapy. *J. Am. Chem. Soc.* **2016**, *138*, 3518–3525.
- (16) Lan, G.; Ni, K.; Xu, Z.; Veroneau, S. S.; Song, Y.; Lin, W. Nanoscale Metal-Organic Framework Overcomes Hypoxia for Photodynamic Therapy Primed Cancer Immunotherapy. *J. Am. Chem. Soc.* **2018**, *140*, 5670–5673.
- (17) Freund, R.; Lächelt, U.; Gruber, T.; Rühle, B.; Wuttke, S. Multifunctional Efficacy: Extending the Concept of Atom Economy to Functional Nanomaterials. *ACS Nano* **2018**, *12*, 2094.
- (18) Lu, K.; Aung, T.; Guo, N.; Weichselbaum, R.; Lin, W. Nanoscale Metal-Organic Frameworks for Therapeutic, Imaging, and Sensing Applications. *Adv. Mater.* **2018**, *30*, 1707634.
- (19) Zhang, K.; Meng, X.; Cao, Y.; Yang, Z.; Dong, H.; Zhang, Y.; Lu, H.; Shi, Z.; Zhang, X. Metal-Organic Framework Nanoshuttle for Synergistic Photodynamic and Low-Temperature Photothermal Therapy. *Adv. Funct. Mater.* **2018**, *28*, 1804634.
- (20) Wuttke, S.; Lismont, M.; Escudero, A.; Rungtaewevoravit, B.; Parak, W. J. Positioning Metal-Organic Framework Nanoparticles within the Context of Drug Delivery - A Comparison with Mesoporous Silica Nanoparticles and Dendrimers. *Biomaterials* **2017**, *123*, 172–183.
- (21) Lismont, M.; Dreesen, L.; Wuttke, S. Metal-Organic Framework Nanoparticles in Photodynamic Therapy: Current Status and Perspectives. *Adv. Funct. Mater.* **2017**, *27*, 1606314.
- (22) Soo Choi, H.; Liu, W.; Misra, P.; Tanaka, E.; Zimmer, J. P.; Itty Ipe, B.; Bawendi, M. G.; Frangioni, J. V. Renal Clearance of Quantum Dots. *Nat. Biotechnol.* **2007**, *25*, 1165–1170.
- (23) Chatterjee, D. K.; Fong, L. S.; Zhang, Y. Nanoparticles in Photodynamic Therapy: an Emerging Paradigm. *Adv. Drug Delivery Rev.* **2008**, *60*, 1627–1637.
- (24) Hatz, S.; Lambert, J. D. C.; Ogilby, P. R. Measuring the Lifetime of Singlet Oxygen in a Single Cell: Addressing the Issue of Cell Viability. *Photoch. & Photobio. Sci.* **2007**, *6*, 1106–1116.

- (25) Pan, L.; Liu, J.; Shi, J. Intranuclear Photosensitizer Delivery and Photosensitization for Enhanced Photodynamic Therapy with Ultralow Irradiance. *Adv. Funct. Mater.* **2014**, *24*, 7318–7327.
- (26) Hu, P.; Wu, T.; Fan, W.; Chen, L.; Liu, Y.; Ni, D.; Bu, W.; Shi, J. Near Infrared-Assisted Fenton Reaction for Tumor-Specific and Mitochondrial DNA-Targeted Photochemotherapy. *Biomaterials* **2017**, *141*, 86–95.
- (27) Yang, Y.; Zhu, W.; Feng, L.; Chao, Y.; Yi, X.; Dong, Z.; Yang, K.; Tan, W.; Liu, Z.; Chen, M. G-Quadruplex-Based Nanoscale Coordination Polymers to Modulate Tumor Hypoxia and Achieve Nuclear-Targeted Drug Delivery for Enhanced Photodynamic Therapy. *Nano Lett.* **2018**, *18*, 6867–6875.
- (28) Liang, P.; Huang, X.; Wang, Y.; Chen, D.; Ou, C.; Zhang, Q.; Shao, J.; Huang, W.; Dong, X. Tumor-Microenvironment-Responsive Nanoconjugate for Synergistic Antivascular Activity and Phototherapy. *ACS Nano* **2018**, *12*, 11446–11457.
- (29) Cavka, J. H.; Jakobsen, S.; Olsbye, U.; Guillou, N.; Lamberti, C.; Bordiga, S.; Lillerud, K. P. A New Zirconium Inorganic Building Brick Forming Metal Organic Frameworks with Exceptional Stability. *J. Am. Chem. Soc.* **2008**, *130*, 13850–13851.
- (30) McKinlay, A. C.; Morris, R. E.; Horcajada, P.; Férey, G.; Gref, R.; Couvreur, P.; Serre, C. BioMOFs: Metal-Organic Frameworks for Biological and Medical Applications. *Angew. Chem., Int. Ed.* **2010**, *49*, 6260–6266.
- (31) Howarth, A. J.; Liu, Y.; Li, P.; Li, Z.; Wang, T. C.; Hupp, J. T.; Farha, O. K. Chemical, Thermal and Mechanical Stabilities of Metal-Organic Frameworks. *Nat. Rev. Mater.* **2016**, *1*, 15018.
- (32) Hu, X.; Sun, J.; Li, F.; Li, R.; Wu, J.; He, J.; Wang, N.; Liu, J.; Wang, S.; Zhou, F.; Sun, X.; Kim, D.; Hyeon, T.; Ling, D. Renal-Clearable Hollow Bismuth Subcarbonate Nanotubes for Tumor Targeted Computed Tomography Imaging and Chemoradiotherapy. *Nano Lett.* **2018**, *18*, 1196–1204.
- (33) Shen, S.; Jiang, D.; Cheng, L.; Chao, Y.; Nie, K.; Dong, Z.; Kutyreff, C. J.; Engle, J. W.; Huang, P.; Cai, W.; Liu, Z. Renal-Clearable Ultrasmall Coordination Polymer Nanodots for Chelator-Free ^{64}Cu -Labeling and Imaging-Guided Enhanced Radiotherapy of Cancer. *ACS Nano* **2017**, *11*, 9103–9111.
- (34) Cheng, L.; Jiang, D.; Kamkaew, A.; Valdovinos, H. F.; Im, H.-J.; Feng, L.; England, C. G.; Goel, S.; Barnhart, T. E.; Liu, Z.; Cai, W. Renal-Clearable PEGylated Porphyrin Nanoparticles for Image-Guided Photodynamic Cancer Therapy. *Adv. Funct. Mater.* **2017**, *27*, 1702928.
- (35) Wang, W.; Ma, Z.; Zhu, S.; Wan, H.; Yue, J.; Ma, H.; Ma, R.; Yang, Q.; Wang, Z.; Li, Q.; Qian, Y.; Yue, C.; Wang, Y.; Fan, L.; Zhong, Y.; Zhou, Y.; Gao, H.; Ruan, J.; Hu, Z.; Liang, Y.; Dai, H. Molecular Cancer Imaging in the Second Near-Infrared Window Using a Renal-Excreted NIR-II Fluorophore-Peptide Probe. *Adv. Mater.* **2018**, *30*, 1800106.
- (36) Wei, Q.; Chen, Y.; Ma, X.; Ji, J.; Qiao, Y.; Zhou, B.; Ma, F.; Ling, D.; Zhang, H.; Tian, M.; Tian, J.; Zhou, M. High-Efficient Clearable Nanoparticles for Multi-Modal Imaging and Image-Guided Cancer Therapy. *Adv. Funct. Mater.* **2018**, *28*, 1704634.
- (37) Liu, K.; Dong, L.; Xu, Y.; Yan, X.; Li, F.; Lu, Y.; Tao, W.; Peng, H.; Wu, Y.; Su, Y.; Ling, D.; He, T.; Qian, H.; Yu, S.-H. Stable Gadolinium Based Nanoscale Lyophilized Injection for Enhanced MR Angiography with Efficient Renal Clearance. *Biomaterials* **2018**, *158*, 74–85.
- (38) Guo, T.; Wu, Y.; Lin, Y.; Xu, X.; Lian, H.; Huang, G.; Liu, J.-Z.; Wu, X.; Yang, H.-H. Black Phosphorus Quantum Dots with Renal Clearance Property for Efficient Photodynamic Therapy. *Small* **2018**, *14*, 1702815.
- (39) Tsvetkova, Y.; Beztsinna, N.; Baues, M.; Klein, D.; Rix, A.; Golombek, S. K.; Al Rawashdeh, W. e.; Gremse, F.; Barz, M.; Koynov, K.; Banala, S.; Lederle, W.; Lammers, T.; Kiessling, F. Balancing Passive and Active Targeting to Different Tumor Compartments Using Riboflavin-Functionalized Polymeric Nanocarriers. *Nano Lett.* **2017**, *17*, 4665–4674.
- (40) Feng, D.; Chung, W. C.; Wei, Z.; Gu, Z. Y.; Jiang, H. L.; Chen, Y.-P.; Darenbourg, D. J.; Zhou, H. C. Construction of Ultrastable Porphyrin Zr Metal-Organic Frameworks through Linker Elimination. *J. Am. Chem. Soc.* **2013**, *135*, 17105–17110.
- (41) Zhang, Y.; Wang, F.; Liu, C.; Wang, Z.; Kang, L.; Huang, Y.; Dong, K.; Ren, J.; Qu, X. Nanozyme Decorated Metal-Organic Frameworks for Enhanced Photodynamic Therapy. *ACS Nano* **2018**, *12*, 651–661.
- (42) Hirsche, P.; Preiß, T.; Auras, F.; Pick, A.; Völkner, J.; Valdepérez, D.; Witte, G.; Parak, W. J.; Rädler, J. O.; Wuttke, S. Exploration of MOF Nanoparticle Sizes Using Various Physical Characterization Methods—Is What You Measure What You Get. *CrystEngComm* **2016**, *18*, 4359–4368.
- (43) Walton, K. S.; Snurr, R. Q. Applicability of the BET Method for Determining Surface Areas of Microporous Metal-Organic Frameworks. *J. Am. Chem. Soc.* **2007**, *129*, 8552–8556.
- (44) Wu, H.; Chua, Y. S.; Krungleviciute, V.; Tyagi, M.; Chen, P.; Yildirim, T.; Zhou, W. Unusual and Highly Tunable Missing-Linker Defects in Zirconium Metal-Organic Framework UiO-66 and Their Important Effects on Gas Adsorption. *J. Am. Chem. Soc.* **2013**, *135*, 10525–10532.
- (45) Fang, Z.; Dürholt, J. P.; Kauer, M.; Zhang, W.; Lochenie, C.; Jee, B.; Albada, B.; Metzler-Nolte, N.; Pöppel, A.; Weber, B.; Muhler, M.; Wang, Y.; Schmid, R.; Fischer, R. A. Structural Complexity in Metal-Organic Frameworks: Simultaneous Modification of Open Metal Sites and Hierarchical Porosity by Systematic Doping with Defective Linkers. *J. Am. Chem. Soc.* **2014**, *136*, 9627.
- (46) Yuan, S.; Qin, J. S.; Zou, L.; Chen, Y. P.; Wang, X.; Zhang, Q.; Zhou, H. C. Thermodynamically Guided Synthesis of Mixed-Linker Zr-MOFs with Enhanced Tunability. *J. Am. Chem. Soc.* **2016**, *138*, 6636–6642.
- (47) Dissegna, S.; Epp, K.; Heinz, W. R.; Kieslich, G.; Fischer, R. A. Defective Metal-Organic Frameworks. *Adv. Mater.* **2018**, *30*, 1704501.
- (48) Fang, Z.; Bueken, B.; De Vos, D. E.; Fischer, R. A. Defect-Engineered Metal-Organic Frameworks. *Angew. Chem., Int. Ed.* **2015**, *54*, 7234–7254.
- (49) Nicolosi, V.; Chhowalla, M.; Kanatzidis, M. G.; Strano, M. S.; Coleman, J. N. Liquid Exfoliation of Layered Materials. *Science* **2013**, *340*, 1226419.
- (50) Coleman, J. N.; Lotya, M.; O'Neill, A.; Bergin, P. J.; King, U.; Khan, K.; Young, A.; Gaucher, S.; De, R. J.; Smith, I. V.; Shvets, S. K.; Arora, G.; Stanton, H.-Y.; Kim, K.; Lee, G. T.; Kim, G. S.; Duesberg, T.; Hallam, J. J.; Boland, J. J.; Wang, J. F.; Donegan, J. C.; Grunlan, G.; Moriarty, A.; Shmeliov, R. J.; Nicholls, J. M.; Perkins, E. M.; Grieveson, K.; Theuwissen, D. W.; McComb, P. D.; Nellist, V.; Nicolosi, V. Two-Dimensional Nanosheets Produced by Liquid Exfoliation of Layered Materials. *Science* **2011**, *331*, 568–571.
- (51) Dai, W.; Dong, H.; Fugetsu, B.; Cao, Y.; Lu, H.; Ma, X.; Zhang, X. Tunable Fabrication of Molybdenum Disulfide Quantum Dots for Intracellular MicroRNA Detection and Multiphoton Bioimaging. *Small* **2015**, *11*, 4158–4164.
- (52) Xu, S.; Li, D.; Wu, P. One-Pot, Facile, and Versatile Synthesis of Monolayer MoS₂/WS₂ Quantum Dots as Bioimaging Probes and Efficient Electrocatalysts for Hydrogen Evolution Reaction. *Adv. Funct. Mater.* **2015**, *25*, 1127–1136.
- (53) Zhu, Y.; Wang, G.; Jiang, H.; Chena, L.; Zhang, X. One-Step Ultrasonic Synthesis of Graphene Quantum Dots with High Quantum Yield and Their Application in Sensing Alkaline Phosphatase. *Chem. Commun.* **2015**, *51*, 948–951.
- (54) Lee, H. U.; Park, S. Y.; Lee, S. C.; Choi, S.; Seo, S.; Kim, H.; Won, J.; Choi, K.; Kang, K. S.; Park, H. G.; Kim, H. S.; An, H. R.; Jeong, K. H.; Lee, Y. C.; Lee, J. Black Phosphorus (BP) Nanodots for Potential Biomedical Applications. *Small* **2016**, *12*, 214–219.
- (55) Ou, H.; Lin, L.; Zheng, Y.; Yang, P.; Fang, Y.; Wang, X. Tri-s-triazine-Based Crystalline Carbon Nitride Nanosheets for an Improved Hydrogen Evolution. *Adv. Mater.* **2017**, *29*, 1700008.
- (56) Wang, H.; Li, P.; Yu, D.; Zhang, Y.; Wang, Z.; Liu, C.; Qiu, H.; Liu, Z.; Ren, J.; Qu, X. Unraveling the Enzymatic Activity of Oxygenated Carbon Nanotubes and Their Application in the Treatment of Bacterial Infections. *Nano Lett.* **2018**, *18*, 3344–3351.

- (57) Li, S.; Zou, Q.; Li, Y.; Yuan, C.; Xing, R.; Yan, X. Smart Peptide-Based Supramolecular Photodynamic Metallo-Nanodrugs Designed by Multicomponent Coordination Self-Assembly. *J. Am. Chem. Soc.* **2018**, *140*, 10794–10802.
- (58) Zou, Q.; Abbas, M.; Zhao, L.; Li, S.; Shen, G.; Yan, X. Biological Photothermal Nanodots Based on Self-Assembly of Peptide–Porphyrin Conjugates for Antitumor Therapy. *J. Am. Chem. Soc.* **2017**, *139*, 1921–1927.
- (59) Meng, X.; Liu, Z.; Cao, Y.; Dai, W.; Zhang, K.; Dong, H.; Feng, X.; Zhang, X. Fabricating Aptamer-Conjugated PEGylated-MoS₂/Cu_{1.8}S Theranostic Nanoplatform for Multiplexed Imaging Diagnosis and Chemo-Photothermal Therapy of Cancer. *Adv. Funct. Mater.* **2017**, *27*, 1605592.
- (60) Cao, Y.; Wu, T.; Zhang, K.; Meng, X.; Dai, W.; Wang, D.; Dong, H.; Zhang, X. Engineered Exosome-Mediated Near-Infrared-II Region V₂C Quantum Dot Delivery for Nucleus-Target Low-Temperature Photothermal Therapy. *ACS Nano* **2019**, *13*, 1499–1510.
- (61) Wang, H.; Yu, D.; Li, B.; Liu, Z.; Ren, J.; Qu, X. Ultrasensitive Magnetic Resonance Imaging of Systemic Reactive Oxygen Species *in Vivo* for Early Diagnosis of Sepsis Using Activatable Nanoprobes. *Chem. Sci.* **2019**, *10*, 3770–3778.